Contents lists available at ScienceDirect

CIRP Journal of Manufacturing Science and Technology

journal homepage: http://ees.elsevier.com

Full-length article

Integrated process simulation of porcelain stoneware manufacturing using flowsheet simulation

C.L. Alves [a,*], A. De Noni Jr [b], R. Janssen [c], D. Hotza [b,d], J.B. Rodrigues Neto [d], S.Y. Gómez González [b], M. Dosta [a]

[a] Institute of Solids Process Engineering and Particle Technology, Hamburg University of Technology (TUHH), 21073 Hamburg, Germany
[b] Department of Chemical Engineering (EQA), Federal University of Santa Catarina (UFSC), 88040-900 Florianópolis, SC, Brazil
[c] Institute of Advanced Ceramics, Hamburg University of Technology (TUHH), 21073 Hamburg, Germany
[d] Graduate Program in Materials Science and Engineering (PGMAT), Federal University of Santa Catarina (UFSC), 88040-900 Florianópolis, SC, Brazil

ARTICLE INFO

Article history:
Available online xxx

Keywords
Flowsheet simulation
Porcelain stoneware
Digitalization
Optimization

ABSTRACT

Integrated simulation of manufacturing plants plays crucial role in development of sustainable processes and optimized products. However, no investigation has been reported for the whole process chain of porcelain stoneware manufacturing. In this contribution, semi-empirical models of porcelain stoneware processing steps have been developed and implemented into Dyssol framework. By validation based on industrial and lab-scale experiments, the simulation has been applied for modeling and sensitivity analysis of the entire process. The simulation results are in a good agreement with experiments showing that the proposed modeling strategy has high potential to be used for future digital transformation in this sector.

© 2021

Nomenclature

Symbol description unit

A
Surface area (m^2)

A_2, B_2, C_2, C_4, C_5
Semi-empirical constants (-)
D
Diameter m
D^{eff}
Effective diffusivity parameter (m^2/s)
d_{32}
Sauter diameter (m)
d_{50}
Median particle diameter (m)
E_a
Activation energy (kJ/mol)
E_m
Specific grinding energy (kWh/kg)
j
Semi-empirical constant (-)
K
Pre-exponential factor (1/m)
L
Length (m)
l_m
Liquid load (-)
m
Semi-empirical constant (-)
$\dot{m}$
Mass flow rate (kg/s)
n
Time factor (-)
P
Power consumed (W)
p
Pressure (N/m^2)
R
Gas constant (J/molK)
r
Radius (m)
T
Temperature (K)

* Corresponding author.
E-mail address: carine.lourenco.alves@tuhh.de (C.L. Alves)

https://doi.org/10.1016/j.cirpj.2021.04.011
1755-5817/© 2021.

UNCORRECTED PROOF

t
Time (s)
t_{sd}
Surface drying time (s)
W_i
Bond work index (kWh/ton)
w_l
Moisture content (kg/kg)
Y
Humidity (-)
z
Height (m)

Greek letters

α
Heat transfer coefficient (W/m^2 K)
β
Mass transfer coefficient (m/s)
c_p
Specific heat (J/kgK)
ϵ
Porosity (-)
μ
Viscosity (kg/ms)
ρ
Density (kg/m^3)
ϕ
Fraction of critical speed (-)

Subscripts

amb
Ambient
at
Atomization
boil
Boiling
drop
Droplet
eq
Equilibrium
f
Feed
gas
Gas
i
Size class i
l
Liquid
mill
Milling
p
Particle
pr
Product
slurry
Slurry

Introduction

In the scope of Industry 4.0, a rapid transformation is currently undergoing towards full digitalization of manufacturing processes [1]. The impact of this industrial revolution is particularly relevant for small and medium sized enterprises with high levels of manual work [2,3]. This is the case of the ceramic industry. Even though ceramic manufacturing processes are highly automated from the point of view of product handling and material processing on the scale of single unit operations, there is no integrative description of them. This lack of integration imposes a limitation for digitalized production, especially in the traditional ceramic sector for manufacturing of porcelain stoneware [2].

Ceramic porcelain stoneware is a high added value traditional ceramic product which is nowadays produced by a sequence of processing steps. There are two main alternative process configurations, so-called "wet" and "dry" routes [3]. In Fig. 1, the "wet" route for porcelain tiles manufacturing consisting of six main unit operations is shown. Depending on the product type, other optional steps such as glazing and design printing can be found in the industrial plants, however they are not considered in this contribution.

There is a variety of studies available for each single unit operation of the entire manufacturing plant [4–10]. Furthermore there are numerous experimental studies investigating the influence of different parameters of single steps on the final product [11–14]. Such studies allow us to improve understanding of occurring processes and reach a high level of standardization of these steps. Barata et al. [15] have pointed out that the high standardization level of the ceramic industry is a barrier towards digitalization, especially due to the extensive experimental material characterization or trial and error approaches carried out for modifications of process parameters. This experimentally-based methodology is time consuming, expensive and does not allow to identify optimal processing parameters with respect to energy or raw material consumption or regarding final product quality. However, given the challenges of the whole plant simulation, there is no study

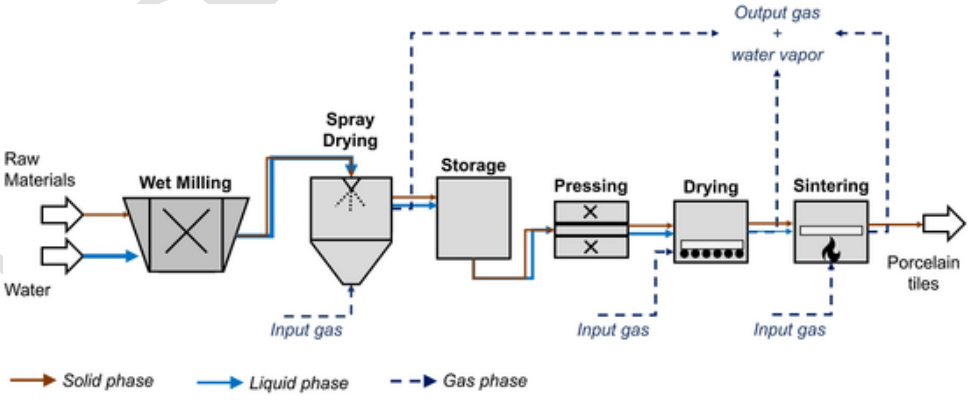

Fig. 1. Flowchart of porcelain stoneware showing the main manufacturing steps.

CORRECTED PROOF

yet available on how the parameters of each separate unit affect the other units and their outcomes throughout the manufacturing chain. It is clear that for the improvement of overall efficiency it is necessary to consider the entire plant, which consists of different steps connected with energy and material streams. In a study for the scientific technological evolution of the porcelain tile industry, Sanchez et al. [17] indicated the limitation of the sector on simulation and modelling tools, even though great technological advances have occurred in the last 30 years on machinery builders. These tools are indispensable to allow the feasibility of processes development, predictability and higher efficiency by innovation in manufacturing, control and measurement [2].

One of the central roles in Industry 4.0 plays numerical simulations, which have become a useful tool to optimize and design industrial equipment as well as to evaluate operation parameters. For numerical investigations of complex plants with the connection of production steps by material and energy streams, the flowsheet calculations can be effectively applied [16]. The flowsheet simulation concept implies the numerical solution of material and energy balances and also the determination of intensive state variables for different process structures [17]. Flowsheet simulation tools are well established in chemical engineering for processes dealing with fluids. However, the use of such tools is not very common yet for processes involving solids, especially ceramic powders. Only in recent years the development and application of such tools for the solid process was initiated [16]. Among the reasons is the high complexity caused due to a more comprehensive description of solids which are described with multi-dimensional distributed parameters. Particles can be distributed along various property coordinates, such as size, density, moisture content, etc. Thus, to perform a correct numerical calculation of material streams described with multidimensional parameters the special approaches like transformation matrices should be applied [18]. For dynamic and steady-state flowsheet calculations of solids processes an open-source simulation framework Dyssol has been developed [17,19]. In this contribution, this system has been extended with new models for different unit operations and applied for simulation of the entire plant.

Another important aspect related to the macroscale process description is the estimation of unknown model parameters. For the flowsheet calculations empirical or semi-empirical models are widely applied. These models contain sets of unknown parameters related to the specific apparatus geometry or material properties. Therefore, for efficient process simulation it is important to adjust these parameters using available experimental data. Alternatively the model parameters can be derived from some microscale calculations [20] or even some data-driven black-box models can be generated [16,20].

In this contribution it is shown how the flowsheet simulation can be effectively applied for macroscale modeling of porcelain tile manufacturing considering different compositions and processing parameters. The simulation allows forecasting the effect and behavior of each unit outcome on the subsequent processes throughout the manufacturing sequence. It is demonstrated that the developed framework is a useful tool to seek optimal conditions for the manufacturing process.

Theory

Every unit operation of the manufacturing plant (Fig. 1) is represented as a separate model in the flowsheet simulation. The models, applied considerations and used numerical methods and algorithms are described in the following subsections. The implemented models are based on previously validated and available in the literature semi-empirical correlations. Appendices A to E provide the information about the adjustment of unknown model parameters that has been performed based on experimental data.

Wet milling

During wet milling, the raw materials are mixed with water and they are grinded in a ball mill for a specific time period to reach desired particle size. To describe the milling process, the flowsheet model based on correlations proposed by Tsakalakis et al. [21] and Morell et al. [22] has been developed. In the first stage, the mass-related specific grinding energy E_m is calculated as a ratio given by the power consumed P to the mill production mass flow $\dot{m}$ as seen in Eq. (1).

$$E_m = \frac{P}{\dot{m}} \tag{1}$$

From known specific grinding energy, initial particle size $d_{50,f}$ and known Bond work index of each single compound W_i, the characteristic particle size $d_{50,pr}$ of the final product is calculated according to Eq. (2).

$$E_m = 0.1169 W_i {d_{50,f}}^{0.193} {d_{50,pr}}^{-0.962} \dot{m} \tag{2}$$

According to Morell et al. [22], the mill power consumption is a function of a no-load power (NLP) and net power (NP), as described in Eq. (3). The factor κ compensates the lost power, such as sound loss, heat transfer, etc.

$$P = (NetPower\,(NP) - NoLoadPower\,(NLP)) \bullet \kappa \tag{3}$$

The no-load power is defined according to Eq. (4), where D is the mill diameter, L is the apparatus length, and ϕ, fraction of critical speed.

$$NLP = 1.68 D^{2.05} [\phi(0.667L)]^{0.82} \tag{4}$$

By combining the correlations proposed by Thorpe [21] and Morell [22], it is possible to estimate the output particle size from milling based on the processing time, power input, apparatus dimensions and material properties. As a simplification, the mill is considered perfectly cylindrical. Furthermore, it is assumed that each solid compound is milled separately and the total grinding energy is distributed between compounds according to their initial volumetric fractions. Finally, the outlet stream is calculated as a mixture of single compounds.

Spray drying

Spray drying is one of the most common methods for the production of a wide variety of particulate products [23,24]. In the scenario of the porcelain stoneware manufacturing, spray drying is performed in a chamber, in which the slurry formed after wet milling is atomized as small droplets using one or several nozzles. The droplets came in contact with a co-current or counter-current hot gas flow and simultaneously occurring heat, mass and momentum exchange result in the formation of granules [25]. Due to the prevalent use of counter-current spray drying in the ceramic industry, this apparatus type has been considered in this work. To increase flexibility during the specification of flowsheet structure, the spray drying model is divided into two sub models to separately represent atomization and drying processes.

Atomization

In the ceramic industry, the atomization is done without additional gas phase by pumping the slurry under high pressure. Therefore, the single fluid atomization model has been implemented. For nozzles with concentric channels, the Sauter diameter size of the droplets d_{32} can be estimated by semi-empirical relationships as shown in Eqs. (5)–(7). The droplet size depends on the nozzle diameter D, liquid load l_m and Ohnesorge number Z_p.

UNCORRECTED PROOF

$$d_{32} = 2 \bullet C_4 \left[\frac{\Delta p \bullet 2D}{\gamma \left(1 + l_m\right)^2} \right]^m \left(1 + C_5 Z_p^j\right) D \tag{5}$$

$$l_m = \frac{\dot{m}_l}{\dot{m}_g} \tag{6}$$

$$Z_p = \frac{\mu_{slurry}}{(\gamma \rho D)^{1/2}} \tag{7}$$

where C_4, m, j and C_5 are the semi-empirical constants, which have been determined based on experimental data [26]. It is assumed that the droplets have a normal size distribution with the median particle diameter equal to the Sauter diameter. The standard deviation is specified by the user as an input model parameter.

Drying of granules

The modelling of spray drying chamber is challenging, given the complexity related to the integration of the drying of the droplets with the interacting hydrodynamic effects as well as heat, mass and momentum transfer between the solid, liquid and gas phases. To describe the drying process, a model based on the correlations proposed by Ali et al. has been developed [23]. This model describes the dependence of particles temperature T_p, moisture content w_l, droplet radius r_p and gas temperature T_{gas} on height z and time. In this one-dimensional plug-flow counter-current model a set of assumptions such as the spherical shape of droplets or neglection of heat transfer by radiation are made. The resulting equations which describe the main thermodynamic states are provided in Eqs. (8) to (11). In all equations, the variables M_x, $c_{p,x}$, T_x denote the mass, specific heat and temperature of component x, respectively.

$$M_{drop} c_{p,drop} v_p \frac{\partial T_p}{\partial z} = \alpha_p A_p \left(T_{gas} - T_p\right) + h_{fg} \frac{dM_l}{dt} \tag{8}$$

$$v_p \frac{\partial w_l}{\partial z} = \frac{\left(1 - w_l\right)^2}{M_{solid}} \frac{dM_l}{dt} \tag{9}$$

$$v_p \frac{\partial r_p}{\partial z} = \frac{dM_l}{dt} (4\pi \rho_{liq} r_p^2) \tag{10}$$

$$\begin{aligned} &\dot{m}_{gas} c_{p,gas} \frac{\partial T_{gas}}{\partial z} \\ &= \sum_{j=1}^{J} \left[\alpha_j A_{p,j} + \frac{dM_{l,j}}{dt} c_{p,vap} \right] \left(T_{p,j} - T_{gas}\right) \frac{\dot{m}_{slurry,j}}{v_{p,j} M_{drop,j}} \\ &\quad + 2\pi R_{app} U \left(T_{amb} - T_{gas}\right) \end{aligned} \tag{11}$$

The heat absorbed by the droplet is the sum of the convective heat flux to the droplet/particle and the heat consumed by the liquid vaporization. The first term depends on the heat transfer coefficient of the droplet α_p, its surface area A_p and the difference between temperatures of the gas and the droplet. The heat consumed in the moisture vaporization is calculated by the product of the latent heat of vaporization h_{fg} and the drying rate ($\frac{dM_l}{dt}$).

Similarly, the temperature of the gas in Eq. (11) is calculated as the sum of the total heat input to the droplets by convection, the sensible heat of the evaporated vapor and heat loss to the environment considering the ambient temperature T_{amb}, where U is the overall heat transfer coefficient. In the first two terms, $\dot{m}_{slurry}$ is the slurry mass flow, v_p is the relative velocity of particles in the gas flow and M_{drop} is the droplet mass.

For simplification, Eq. (11) is solved for only one representative droplet diameter which is equal to the Sauter diameter obtained from the atomization model. This size is adopted to perform all the calculations and to obtain the respective size reduction due to moisture evaporation. Afterwards the obtained percentile of reduction is applied for the whole distribution of granules size.

The droplet drying rate dM_l/dt varies through three different drying stages. In the first drying stage, the residence time is smaller than the surface drying time t_{sd}, the drying rate is calculated by Eq. (12). The surface drying time is taken as the time which is needed to reduce the moisture concentration at the surface to a 90% of the equilibrium moisture content. The drying rate on this stage depends on the saturated humidity of the gas Y_{sat}, the current gas humidity Y, mass transfer coefficient β and the surface area of the droplet/particle given by its radius r_p .

$$\frac{dM_l}{dt} = -4\pi r_p^2 \beta (Y_{sat} - Y) \tag{12}$$

Once the surface is dry ($t > t_{sd}$), the drying rate is limited by the internal diffusion of moisture to the surface. In this period, the rate calculated as:

$$\frac{dM_l}{dt} = -10^6 r_p exp\left[-18.9 \left(\frac{t - t_{sd}}{10^6 r_p} \right)^{0.2} - 17.7 \right] \tag{13}$$

The third drying stage starts when the particle temperature reaches the boiling point of the slurry T_{boil}. In this case the drying rate is calculated according to Eq. (14), where $\frac{dT_{boil}}{dw_l}$ is the variation of the boiling temperature of the slurry in relationship with the moisture content.

$$\frac{dM_l}{dt} = -\frac{\alpha_p 4\pi r_p{}^2 \left(T_{gas} - T_p\right)}{h_{fg} - ((1 - w_l) c_{p,solid} + w_l c_{p,liq})(1 - w_l) \frac{dT_{boil}}{dw_l}} \tag{14}$$

For the implementation of the spray drying model, the spray tower has been discretized through a height into a set of layers. In the first iteration, the output gas temperature has been assumed to be equal to the initial temperature of granules. Using this assumption, the calculations have been performed from the top to the bottom of the tower. The numerical calculation of the derivatives in Eq. (8) to (11) is made by the finite difference method for every height layer. Finally, the calculated gas temperature at the bottom of the tower is compared with the known value of inlet gas temperature. If there is a substantial deviation between these temperatures, the assumed value of the outlet gas temperature is slightly increased and the calculations are repeated. The average number of iterations needed to reach convergence is about 12 iterations.

The final moisture distribution over the different particle sizes classes has been calculated based on two assumptions. Firstly, it is assumed that the moisture content of each granule is proportional to its size. The second assumption is that the moisture evaporation occurred by a drying front and all granules have the same dry layer thickness.

Storage

During storage, the granules obtained from spray drying are collected and stored in industrial silos with 10–13 m height. The large granules formed after spray drying have higher moisture content compared to smaller ones [27] and as a consequence the granules reveal different mechanical behavior. This can negatively influence the quality of conformed green bodies and lead to formation of zones with different densities. Consequently, to avoid this problem, one of the main goals during storage is to ensure complete moisture homogenization among the grains.

UNCORRECTED PROOF

Industrially, the silos are fed centrally which means that the atomized powder is directed through conveyor belts to the top of the silo, where it is dumped inside. This feeding system is adopted in the model and it is also assumed that there is no moisture evaporation during storage.

To describe moisture homogenization during the storage a mass transfer model is developed. For particles from each size class i, the variation of the moisture W_l over time is calculated according to:

$$\frac{\partial W_{l,i}}{\partial t} = \beta \pi d_i^2 \left(\bar{W}_l - W_{l,i}\right) \tag{15}$$

where d_i is the diameter of granules from size class i, β is the mass transfer coefficient and $\bar{W}_l$ is the average moisture content in the silo. The mass transfer coefficient has been fitted according to experimental data [26] (s. Appendix B).

To perform the calculation of moisture homogenization the total storage time τ_{stor} is discretized into smaller time steps Δt and in each time step the predictor-corrector scheme is applied to ensure the conservation of mass. It is ensured that at any arbitrary time point the summarized liquid mass flow which leaves wet granules $\dot{m}_{l,giv}$ is equal to the summarized mass flow that is received by more dry granules $\dot{m}_{l,rec}$. In the predictor step, the change of the moisture content from the particles of size class i is calculated according to Eq. (15). If the value calculated is negative it is summed to the received mass flow $\dot{m}_{l,rec}$, otherwise it is summed to the given mass flow $\dot{m}_{l,giv}$. Afterwards, the overall mass flow of transferred liquid $\dot{m}_l$ is determined as the minimum value between the absolute values of the received and given mass flow. This condition assures that the liquid mass transferred between granules is conserved. In the corrector stage the normalization of equations to describe time-dependent moisture change is performed. Fig. 2 illustrates the main flowchart of the developed calculation algorithm.

Pressing

The most widely applied shaping method for stoneware is dry pressing due to the low costs and high productivity. The granules after storage are compacted in a rigid cavity by applying pressure in only one axial direction through a rigid punch forming the green tile. The main process control parameter is given by the bulk density of the tile, which can be translated by porosity content. There exist several correlations to describe influence of applied pressure on the porosity [28,29]. One of the most widespread models used is the semi-empirical one proposed by Bal'shin et al. [28]. Here the porosity of the tile ε depends on the density of the atomized powder ρ_{at}, applied pressure p and parameters A_2 and B_2, as it is shown in Eq. (16).

$$\varepsilon = 1 - \frac{\rho_{at}}{A_2 lnp - B_2} + C_2 d_{50,mill} \tag{16}$$

The second term, with an additional parameter C_2 and which considers the influence of median particle size obtained after milling $d_{50,mill}$, has not been considered in the original model of Bal'shin. This modification is proposed based on experimental data and previous work of the authors [30,31].

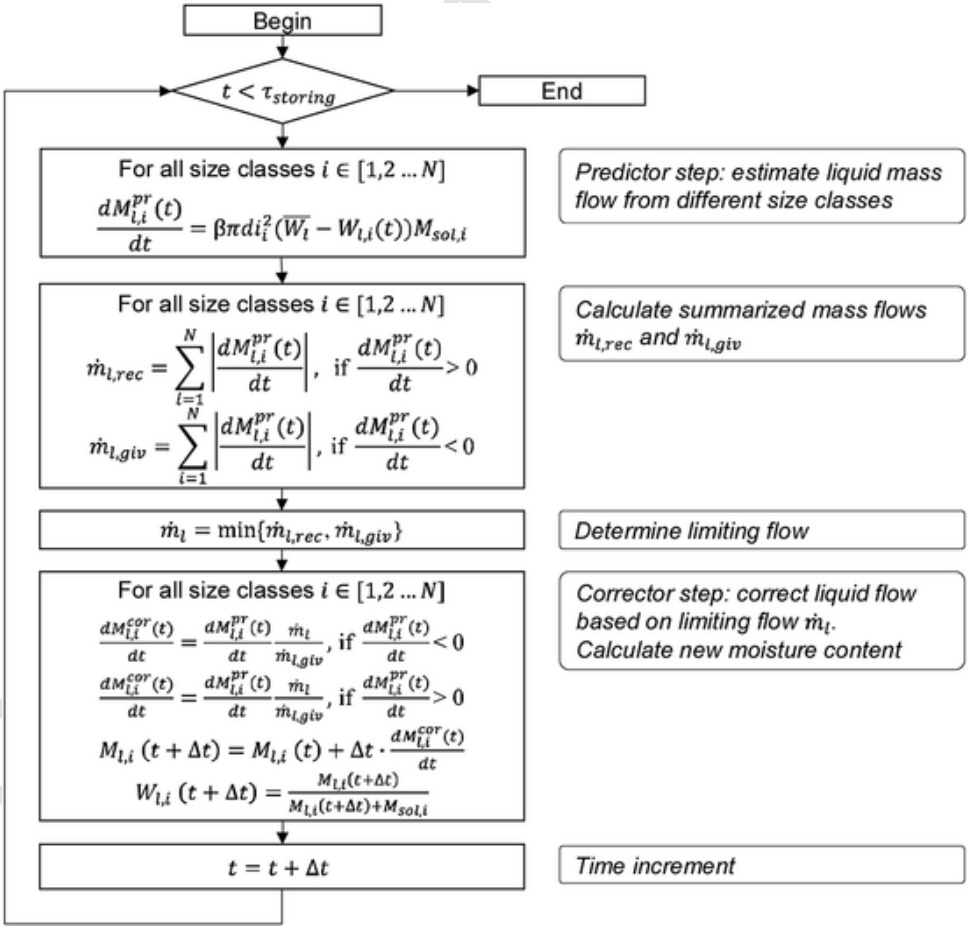

Fig. 2. Flowchart of the algorithm to calculate time-dependent moisture distribution.

Drying

The main goal of the drying process is to reduce the moisture content of the tile from 6 to 8% to approximately 1%. This is made in industrial convective dryer through hot gases circulation. It is generally agreed in the literature that the moisture distribution within a grain over time is controlled by diffusion as stated by Fick's law given by Eq. (17) [32–38], where D^{eff} is the effective diffusivity parameter.

$$\frac{\partial W_l}{\partial t} = \nabla(D^{eff}\nabla W_l) \tag{17}$$

The mathematical solution of this equation can be derived by several conventional (thin layer equations, Fourier's equations) and non-conventional approaches like neural networks [37]. In this contribution, thin layer equations have been adopted. Such lumped parameter model addresses the thin layer drying as only layer of sample particles or slices and due to the thin structure of layers, the temperature distribution can be assumed as uniform [32].

Henderson et al. [39,40] used the thin layer approach and derived the analytical solution given in Eq. (18). This model has also been used in finite element method calculations [41].

$$\frac{W_l(t) - W_{l,eq}}{W_l(0) - W_{l,eq}} = A_1 exp\left(-\frac{\pi^2 D^{eff} t}{A_2}\right), \tag{18}$$

where $W_l(0)$ is the initial moisture content of tile considered to be homogeneous in the entire geometry and $W_l(t)$ is the average moisture content in the tile at a time t. $W_{l,eq}$ is the equilibrium moisture content, at which the tile is neither gaining nor losing moisture. $W_{l,eq}$ depends on the material, relative humidity and air temperature and is assumed to be 10^{-4} for porcelain tile [42,35]. The parameters A_1 and A_2 are geometric constants which depend on the geometry of the green body. Considering the thickness of green body L, Eq. (18) can be rewritten as:

$$\frac{W_l(t) - W_{l,eq}}{W_l(0) - W_{l,eq}} = 1 - 8/\pi^2 exp\left(\frac{-\pi D t}{L^2}\right) \tag{19}$$

Sintering

Densification by sintering is achieved in a process often termed as firing. This allows to minimize porosity and to obtain a resistant tile. Specifically, an isothermal regime of the process has been investigated in this work and tile porosity is described with correlation proposed by Gómez et al. [43]. The dependency between median particle size $d_{50,mill}$ obtained after milling and porosity ε is calculated as:

$$\varepsilon = \varepsilon_0 exp\left[-\frac{k}{d_{50,mill}} t^n exp\left[\frac{-E_a}{RT}\right]\right], \tag{20}$$

where k and n are the frequency and time factors accordingly, E_a is the activation energy, R is the gas constant, T is the temperature, t is the time and ε_0 is the porosity of the green body obtained after pressing. The values of n, E_a and k have been estimated based on previously obtained experimental data. However, since experiments have been performed for constant heating rate, the correlation given in Eq. (21) is firstly applied to estimate unknown parameters and only afterwards Eq. (20) is used for modeling of the manufacturing process.

$$\varepsilon = \varepsilon_0 exp\left[-\frac{nRk}{d_{50,mill}\, E_a} t^n exp\left[\frac{-E_a}{R\left(T_0 + \beta t\right)}\right]\right], \tag{21}$$

where T_0 is the initial temperature and β is the heating rate. A detailed description of procedure to find unknown model parameters is provided in Appendix E.

Material and methods

The described above semi-empirical models for the apparatuses and processing steps have been implemented into the open-source flowsheet simulation framework Dyssol [44]. The material database of Dyssol has been extended to consider the properties of two different compositions which are listed in Table 1. For this purpose, the porcelain constituents such as feldspar, clay, kaolin, etc. have been added. The thermo-mechanical properties of these constituents depend directly on the oxides content [35]. Based on the composition provided in Table 1 and the values provided in the literature [42,34], the required properties of all six components have been defined. It should be noted, that the *Composition 1* also contains quartz however it is not explicitly specified but implicitly included into all three main constituents.

To describe particle size distribution (PSD) for both compositions the equidistant grid from 0 to 5 mm containing 1000 size classes has been applied for process simulation. The PSD of all raw components has been described as a normal distribution with given median d_{50} and standard deviation σ.

Table 2 summarizes the main process parameters for the porcelain manufacturing of *Composition 1* that are used for flowsheet simulation.

The *Composition 1* and corresponding process parameters provided in Table 2 have been defined based on the data obtained from the Brazilian porcelain factories: "Eliane Revestimentos Cerâmicos" and "Cecrisa Revestimentos Cerâmicos". The experimental data which have been used to estimate unknown model parameters and to validate models have been obtained from new experimental measurements and previous contributions [45,30,46,26,31]. This data has also been derived for the abovementioned factories with same process conditions. For almost all models of single unit operations industrial data has been used. However, due to the difficulties of obtaining and adjustment of sintering parameters for industrial kiln, the model parameters of Eq. (20) have been estimated based on data of a laboratory scale kiln (Electric furnace Jung LT 3). In this case, the simulation of sintering in the lab-scale kiln has been performed with Eq. (21) and compared with experi-

Table 1
Two different compositions of the raw materials.

	Composition 1			Composition 2		
Oxides	Feldspar	Clay	Kaolin	Wollastonite	Alumina	Quartz
Mass fraction [%]	50	25	25	26	37.9	36.1
SiO_2 [%]	76.34	59.41	66.36	52.0	0.02	99.0
Al_2O_3 [%]	14.25	25.28	22.53	1.0	99.5	
Na_2O [%]	4.52	0.87	0.21			
K_2O [%]	1.85	1.62	2.70	0.2		
MgO [%]	0.44	0.89	0.14			
Fe_2O_3 [%]	0.23	1.19	0.82	0.25	0.020	0.05
Li_2O [%]	0.73					
CaO [%]				43.2		
MgO [%]				1.0		
Na_2O [%]				0.2	0.3	
TiO_2 [%]					0.007	
Others [%]	0.86	1.30	0.38			
Fire loss	1.51	8.23	6.92			
d_{50}[μm]	100	20	25	22	4.6	5.3
σ [μm]	10	10	10	17.4	3.2	2.6

UNCORRECTED PROOF

Table 2
Main process parameters of all units for processing of Composition 1.

Unit	Process parameters	
Wet milling	Conventional industrial ball mill	
	Processing time [h]	5
	Mill diameter [m]	2.2
	Mill length [m]	6.5
	Power input [kWh/ton]	58
	Fraction of critical speed [-]	0.5
	Water fraction [-]	0.64
Spray drying	SACMI ATM 65	
	Chamber height [m]	10
	Half spray angle injection [°]	90
	Nozzle radius [mm]	3
	Gas flow rate [kg/s]	0.3
	Gas input temperature [°C]	600
	Slurry flow rate [kg/s]	7.3
	Insulation thickness [m]	0.02
	Column wall thickness [m]	0.01
Storing	Industrial silo	
	Storage time [h]	48
	Silo height [m]	15.1
	Silo diameter [m]	4
Pressing	Hydraulic press SACMI PH9800	
	Length [m]	0.84
	Width [m]	0.84
	Thickness [mm]	11
	Pressure [MPa]	45
Drying	Vertical EVA902	
	Drying time[h]	0.42
	Gas temperature [°C]	200
Sintering	Electric furnace Jung LT 3	
	Mode	single burn
	Sintering time [s]	400
	Sintering temperature [°C]	1220

mental data. Afterwards, adjusted model parameters have been used in Eq. (20) for industrial sintering times and temperatures.

A porcelainized stoneware *Composition 2* for anorthite is based on data from Taskiran et al. [47] and has been used to validate models for wet milling and sintering. The process parameters have been also taken from Taskiran et al. [48]. Appendix F describes in details the process parameters and considerations made for the simulations.

Results and discussion

Process simulation

The entire plant has been simulated in steady-state mode and simulation results have been compared to the experimental data. In Fig. 3 the particle size distributions at different stages of the manufacturing process are shown. The initial raw materials with median size of 60 μm have been milled that lead to reduction of median particle size to 10.1 μm. Due to the different material strengths, the components milled differently attaining different sizes. The average diameter of feldspar decreased from 100 to 16.4 μm. The average diameter of clay diminished from 22 to 4 μm and of kaolin from 32 to 4.9 μm. Within the spray drying process, granules with average diameter of 307.1 μm are formed.

In Fig. 4 (a) and (b), the schematic representation of counter-current spray dryer and thermodynamic properties in it are shown. It can be observed that the gas temperature and moisture are non linearly dependent on the vertical position. The droplets injected at the top of the dryer contact humid gas with relatively low temperatures, leading to moderate drying rates. At the bottom of the chamber, where the pre-heated droplets contact the high-temperature inlet gas, the higher evaporation rate can be observed.

In Table 3, various properties such as moisture, porosity and median particle size are listed. Overall, it can be seen that after the adjustment of model parameters which are described in detail in Appendix A, the simulation results are in good agreement with experimental data.

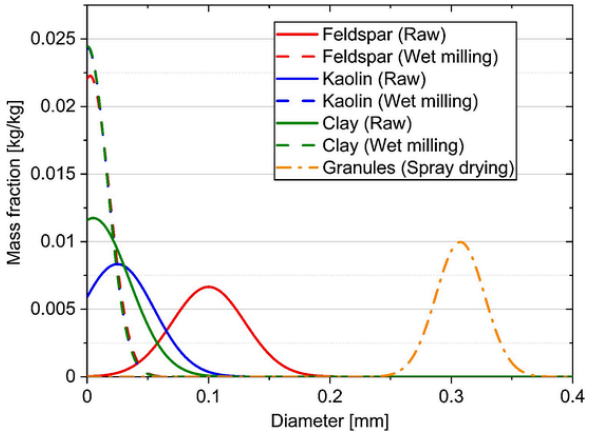

Fig. 3. Particle size distribution throughout process chain.

UNCORRECTED PROOF

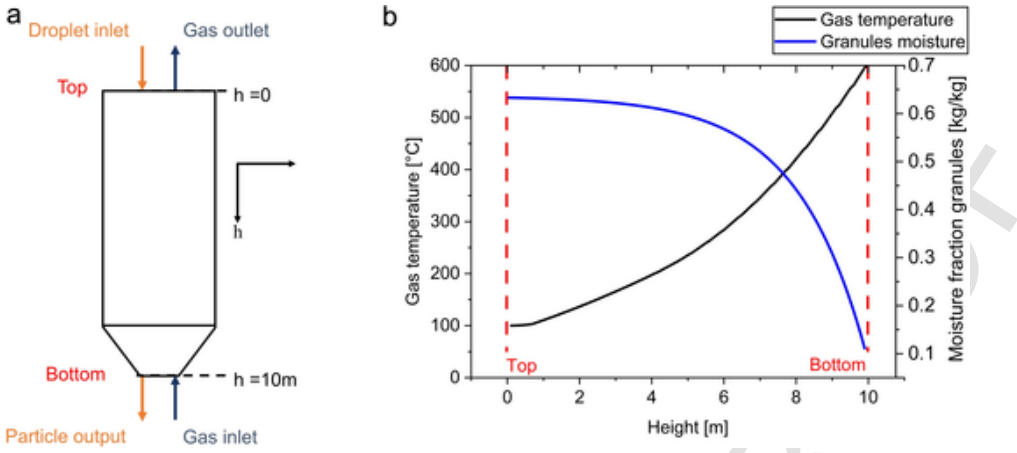

Fig. 4. (a) Counter-current spray drying configuration scheme (b) Profile of the gas temperature and granules moisture during spray drying.

Table 3
Comparison between experimental data and simulation results.

Unit operation	Property	Experiments	Simulation
Wet milling	Particle diameter (d_{50}) [μm]	11.23	11.3
Spray drying	Granules temperature [°C]	60	58.2
	Gas output temperature [°C]	100	100
	Moisture [%]	7	7
	Granule diameter (d_{50}) [μm]	311	307
Storage	Moisture [%]	6.5	7
Pressing	Porosity [%]	33	32.9
Drying	Moisture [%]	0.3	0.31
Sintering	Porosity [%]	3.5	3.49

Existing literature suggests that flowsheet process simulations can be computationally expensive and potentially inaccurate. These problems are given by the high dimensional equations systems that are often highly nonlinear, ill-conditioned and poorly structured [49,50]. These issues are often directly related to the robustness of numerical algorithms, which may hinder transfer of research advances to final software products and, as a consequence, strongly limit their industrial applicability. These matters could be overcome in this study and an industrial application can be foreseen. The overall calculation time needed to perform flowsheet simulations in Dyssol and to reach steady-state is in the range of 4 s.

With the proposed flowsheet model, it is possible to analyze the influence of parameters of single unit operations parameters not only locally, but through the whole process chain. Fig. 5 shows the influence of specific parameters on the entire manufacturing process.

The material properties that have a major influence on the entire process behavior are the particle size obtained after milling, the moisture of granules and green tile porosity. Based on that, a sensitivity analysis is carried out at different case studies where only one of the following parameters is modified at the same time:

- Milling time
- Pressure applied during pressing
- Sintering time and temperature.

In the real process, the moisture obtained after spray drying will depend on various properties, such as diameter of particle obtained after milling. However, this is not considered in this contribution, since it would require a previous knowledge of the influence of temperature and pressure on diffusivity parameters of the slurry with specified chemical composition.

Sensitivity analysis

Three case studies are presented in the following sections considering the variation in the milling, pressing and sintering, on the properties of the output of units along the porcelain stoneware manufacturing process.

Variation of milling time

The milling step directly impacts the PSD of the slurry and consequently of the granules that are conformed into the tile. The influence of milling time on the median diameter in the slurry can be seen in Fig. 6. Since more energy is invested for comminution, the values of d_{50} decrease with increasing milling time. A good agreement between experiments from literature and simulation can be observed, where R^2 value is equal to 0.96 and mean absolute difference of1.36 microns. The typical industrial milling time is in the range from 3 to 5 h [46]. In this range the difference between experimental and numerical results reduces to 0.59 microns. For longer time intervals the model slightly overpredicts the milling process.

The influence of milling time on the green body density and final tile porosity is investigated for the industry-relevant time interval from 3 to 5 h. Fig. 7 shows comparison between simulation results and experiments. It can be observed that longer milling intervals lead to higher porosity of the green body after pressing. With decreasing particle size, the attractive forces and interparticle friction is increased leading to enhanced agglomeration of particles [51]. Strong agglomeration compromises the fluidity of the particles in the die during conformation and it leads to the formation of large pores and, thus, higher porosity. Contrary to this, the opposite influence of milling time on porosity of the final product can be observed. According to Carter et al. [52] the kinetics of sintering is governed by the reactant particle size. On the one hand, fine particles mostly promote the reaction because of the decreased distances. On the other hand, the growth of the solid-state reaction product in powder systems essentially occurs at particle contact

UNCORRECTED PROOF

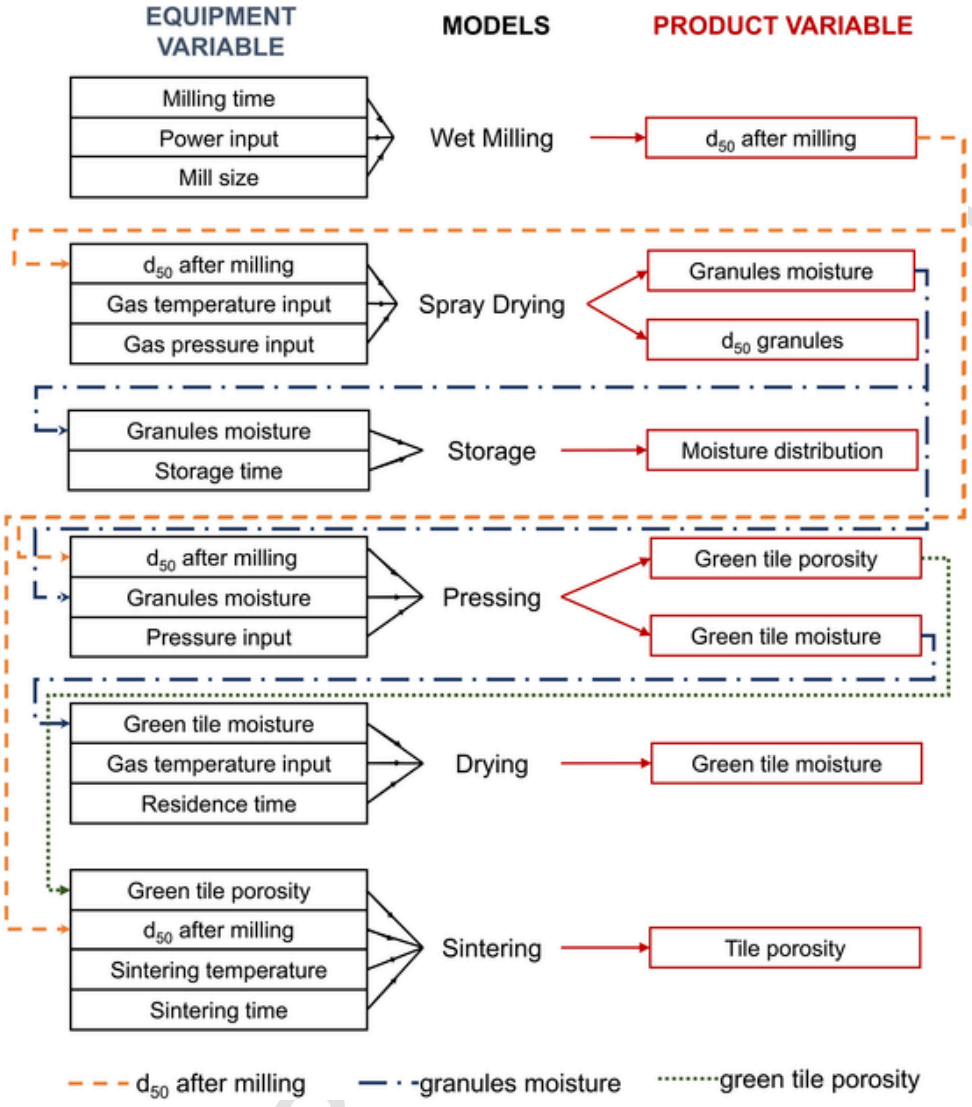

Fig. 5. Interdependency of different process parameters in the entire plant.

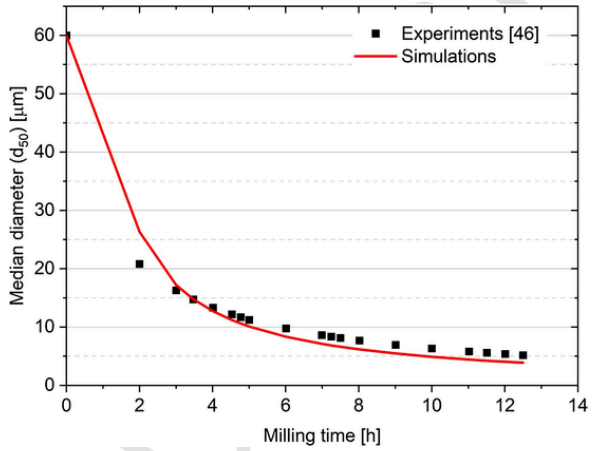

Fig. 6. Influence of the median particle diameter in slurry on milling time. Experimental data from Darolt et al. [46].

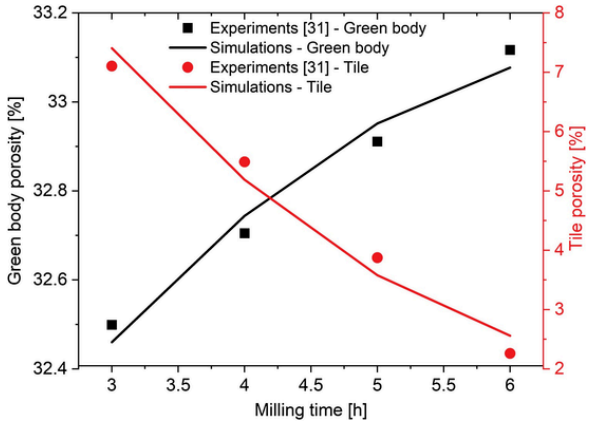

Fig. 7. Influence of milling time on porosity of the green body and porosity of the sintered tile. Experimental data from De Noni et al [31].

points. Thus, the combined effect of reactant particle size and degree of green body particle contacts (variation in green porosity) directly affects the porosity after sintering. The increased contact among particles created by agglomeration, leads to smaller tile densities [53,54]. Therefore, to increase the density of the tiles, it is mandatory that the green bodies possess low green density and homogenous packing of particles.

The same conclusion has been drawn for different porcelain compositions. Taskiran et al. [47,48] developed a porcelainized stoneware composition based on anorthite and performed an extensive detailed experimental study of the influence of milling time on the sintering behavior. The data obtained by experiments according to the study of Taskiran et al. [48] and simulation of *Composition 2* (s. Table 1) for different milling time is presented in Fig. 8 (a). The influence of the milling times on the porosity after sintering at 1225 °C can be seen in Fig. 8 (b). Detailed information on the chemical composition of this formulation and processing parameters is provided in Appendix F.

A good agreement between experiments and simulation has also been obtained considering *Composition 2* with an average difference value of 1.25 microns. However, it can be observed that longer milling times result in a higher discrepancy of experimental and numerical results. Moreover, for the same sintering temperature, the porosity after sintering decreased with higher milling times.

Overall, the good agreement between experimental data and simulation results for different compositions and processing conditions allows to forecast outcomes of individual processing units and of the final product, without the need of expensive experimentation or trial and error approaches.

Pressure variation during pressing

The properties of the final porcelain tile strongly depends on the microstructure of the green body [55]. Fig. 9 illustrates the effect of applied pressure on the porosity of the green tile. A good agreement has been obtained after to the adjustment of A_2 and B_2 model parameters (Eq. (16)) for granules with different moistures, as seen in Appendix C. The good match between experiments and simulation is confirmed by the R^2 value of 0.99.

The porosity of the green body decreases when higher pressures are applied or when the moisture of the granules is increased. The moisture favors the formation of intergranular bonding. Tanaka et al. [56] showed that more intensive local particle rearrangement might occur with higher moisture content, enhancing the particle packing in the green body.

The influence of pressure applied during conformation on final tile porosity has been investigated in the interval between 40 and 50 MPa. This is a common range of pressures applied for the stoneware conformation in the industry [57,3,55]. The influence of pressure on porosity of the green tile prior to sintering as well as on the end porosity of the tile are shown in Fig. 10. It can be inferred that an increase in pressure leads to almost linear decrease in both properties. Nevertheless, the absolute porosity reduction on sintering is approximately 10 times smaller than the reduction of porosity after pressing. This behavior is consistent with the well-known fact that the final density is essentially influenced by the sinterability of the system, e.g. by particle size and phase composition. The simulation, thus, allows to forecast the porosity after sintering for specified conditions.

Time and temperature variation during sintering

The reduction of porosity during sintering depends on several variables such as temperature, time, initial density and particle size [43,58]. Firing temperature and time are determining factors in obtaining appropriate technical properties of porcelain stoneware. Experimental data obtained by single burn conventional sintering for *Composition 1* has been used to analyze the behavior of this unit. In the experiments the fixed heating of 50 °C/min until 450 °C, followed by a rate of 30 °C/min until the plateau was used. Four different plateau holding time intervals of 3, 5, 10 and 15 min as well as different plateau temperatures in the range of 1120 °C and 1260 °C was considered [30]. The model is applied during the isothermal period to compare the sintering model proposed by Gómez et al. [43]. The minimum porosity achieved by experiments and simulations is equal to 0.054 %. A good agreement with R^2 value of 0.94 is obtained considering the different conditions of holding temperatures and times, presenting slight discrepancy at temperatures above 1180 °C as seen in Fig. 11. This is caused due to the fact that the feldspar develops a liquid phase at low temperatures about 900 °C [3,59]. Due to the high amount of this component, there is a high amount of liquid (ca. 50–60 %) leading to a blowing effect. This justifies the increase of closed porosity observed in the experiments for all sintering times evaluated for temperatures higher than 1180 °C.

Considering the analysis carried by Tsakiran et al. [48], the sintering process for *Composition 2* has been evaluated for test samples on temperatures ranging from 1160 to 1325 °C with 25 °C intervals and soaking time of 3 h. Different milling times have been considered for the analysis ranging from 3 h, 12 h, 24 h, 48 h and 96 h. The comparison between experiments and simulation can be seen in Fig. 12. A good agreement has also been obtained with R^2 value of 0.95 with an average difference of 0.3 %. Considering both compositions, it is possible to analyze different processing parameters and outcomes from units through the developed models. In the case of the second composition, the optimal milling time is 48 h and sintering temperature is 1200 °C, that allows to reach almost zero porosity. Further milling and higher sintering temperature would lead to inefficient utilization of energy in the process. This conclusion has been drawn by Taskiran et al. [48] with extensive experimental work. The same outcome has been derived by the simulation with according processing parameters for the milling and sintering units.

Considering the *Composition 2* proposed by Tsakarian et al. [48], the blowing effect has occurred in temperatures higher than 1240 °C but not as significant as in the *Composition 1*. Consequently, the influence of the blowing effect is more significant for this composition, justifying the higher divergence from simulations. The simulation for *Composition 2* overestimates the porosity for milling times above 12 h. This is caused due to discrepancies which already appear in the wet milling and propagates through the whole process chain.

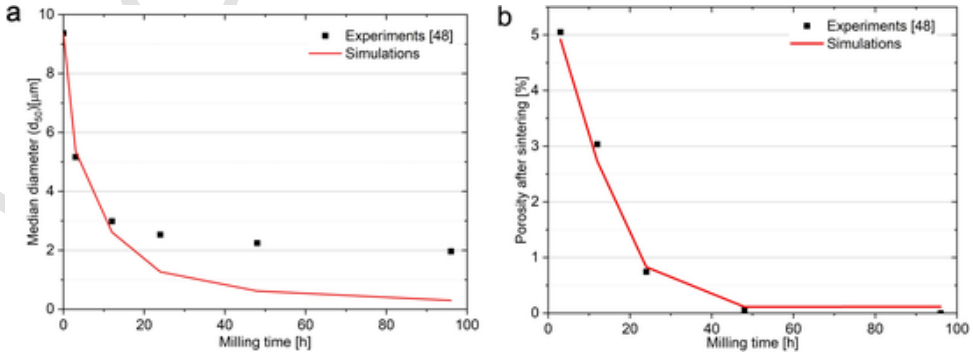

Fig. 8. Comparison between the experimental study of Taskiran et al. [48] and new simulations.

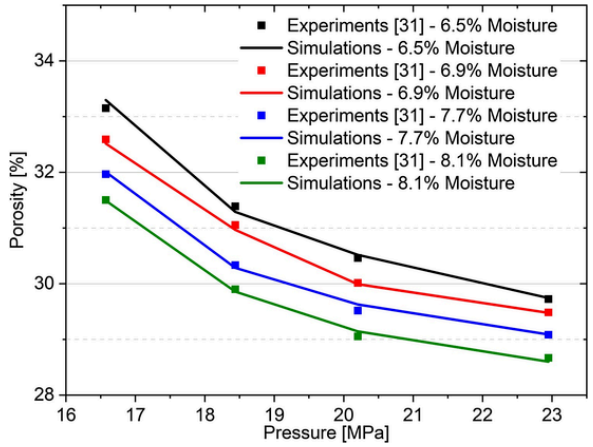

Fig. 9. Comparison between simulation and experiments of porosities obtained after pressing for different pressures applied and granules moisture. Experimental data from De Noni et al [31].

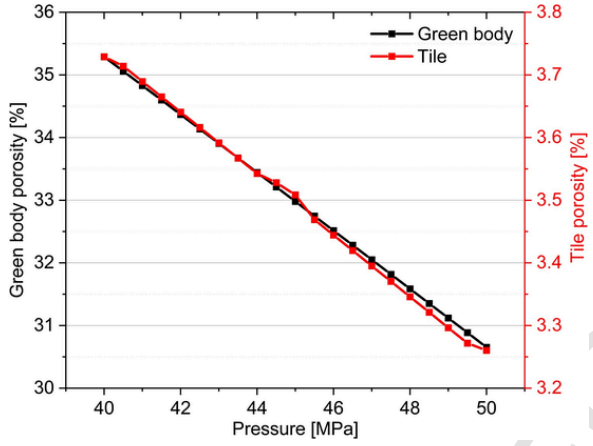

Fig. 10. Correlation between the porosity of the green body and sintered tile for different pressures applied during pressing.

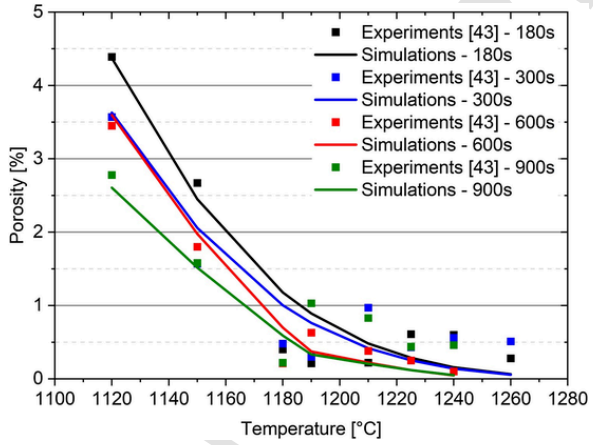

Fig. 11. Comparison of the evolution of porosity on the tile for different sintering times and temperatures. Experimental data from Gómez et al. [43].

The sintering model implemented here has been developed for alumina solid-state sintering considering only open porosity and disregarding the effect of liquid phases during sintering. It is supposed that there is a direct correlation of the sintering mechanism with the values of the time factor parameter (n), which may lead to the different values found. However, the development of a sintering model for porcelain tiles including these aspects is beyond the scope of this work. It is envisioned that a microscale calculations approach like the discrete element method can allow to include these aspects [60,12].

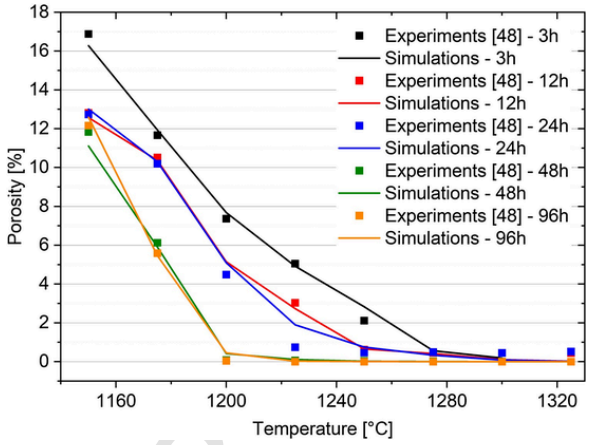

Fig. 12. Comparison of simulations and experiments of sintered tile porosity for different milling times based on data of Tsakiran et al. [48].

Conclusion and outlook

An integrated flowsheet process model for porcelain stoneware manufacturing process has been developed and applied for simulation of an entire plant. Semi-empirical models of all relevant processing steps, such as milling, spray drying, pressing, sintering, etc. have been developed and implemented to the flowsheet simulation framework Dyssol. The unknown model parameters were adjusted based on the lab-scale or industrial experimental data.

The proposed flowsheet model has been successfully used to consider interdependencies between single unit operations in the whole process chain and to analyze the influence of main process parameters. It was shown how milling time, pressure applied during pressing and sintering parameters influence process state or final product properties. Overall, it was shown that simulation results are in a good agreement with experimental data considering different compositions and processing parameters. Furthermore, the flowsheet simulation and Dyssol demonstrated to be effective in establishing a digital twin of ceramic fabrication, allowing to forecast outcomes during the processing sequence without the need for extensive experimentation or trial and error approaches. This offers the potential to perform sensitivity analysis throughout the process chain, to determine optimal parameters and as a consequence to make step towards process sustainability.

Declaration of interests

The authors declare that they have no known competing financial interests or personal relationships that could have appeared to influence the work reported in this paper.

Acknowledgments

We gratefully acknowledge the financial support of the German Research Foundation (DFG). Project-ID: 418788750 (DFG DO 2026/6-1), of the DAAD (Pro Bral 57447192) and of CAPES-DFG program (PIPC 88881.207634/2018-01).

Appendix A. Parameters adjustment

The presented above semi-empirical models of different transformation steps starting with wet milling and ending with sintering contain-

ing a set of unknown parameters. These parameters were adjusted according to the experimental data using a generalized reduced gradient and the Levenberg-Marquardt algorithm. The estimated model parameters for all unit operations are listed in Table A1. Table A2 shows additional material properties and model parameters used for calculations.

Appendix B. Storage parameters

To adjust the mass transfer coefficient experimental data from Demarch et al. [26] has been used. In their study the granules obtained by spray drying have been stored in a silo of 200 m^3. A sample powder of 100 g has been collected from the silo discharge for every hour, and then the granulometric and moisture distribution has been determined. The moisture of the granules has been measured based on their mass. For size analysis, sieving has been made with 5 meshes with cut size of 500 μm, 425 μm, 300 μm, 212 μm and 125 μm. The material retained on the meshes 500 and 425 μm has been considered as coarse granules, medium granules on the meshes 300 μm and 212 μm and fines on the 125 μm. Assuming that the coarse granules have initially the highest moisture content, the evolution of moisture homogenization has been evaluated as moisture difference between fine and coarse granules. The homogenization degree $Y(t)$ comparison between experiments and simulation is shown in Fig. B1. This degree is calculated as:

Table A1
Parameters of the models fitted to the experimental data.

Processing step	Parameter	Value
Wet milling	Power correction (κ)	$1.8{\cdot}10^{-1}$
Atomization	Constant C_4	1
	Constant C_5	2.55
	Constant m	$-4{\cdot}10^{-1}$
	Constant j	1
Spray drying	Diffusivity coefficient of water in slurry [m/s]	$3{\cdot}10^{-11}$
Storing	Mass transfer coefficient (β) [m/s]	$6.5{\cdot}10^{-5}$
Pressing	A_2	$5.52{\cdot}10^{-2}$
	B_2	$8.54{\cdot}10^{-1}$
	C_2	$2.53{\cdot}10^{-3}$
Drying	Diffusivity constant (D) [m^2/s]	$5.06{\cdot}10^{-8}$
Sintering	Pre-exponential value (k) [-]	$6.46{\cdot}10^{5}$
	Activation energy (E_a) [kJ/mol]	275 kJ/mol
	Time factor (n) [-]	1.84

Table A2
Additional material properties and model parameters used for calculations.

Processing step	Parameter	Value
Atomization	Differential pressure at the nozzle [Pa]	$2.45{\cdot}10^{6}$
	Surface tension of liquid on slurry [N/m]	$7.28{\cdot}10^{-2}$
	Viscosity [Pa•s]	0.5
Spray drying	Thermal conductivity wall [W/mK]	18.8
	Thermal conductivity insulation [W/mK]	$4{\cdot}10^{-2}$
	Gas velocity [m/s]	9.25
	Specific heat of vapor slurry [J/kgK]	1900
	Diffusivity coefficient of water vapor in air [m^2/s]	$7.5{\cdot}10^{-4}$
	Latent heat of vaporization of water [J/kg]	$2.5{\cdot}10^{6}$
Storing	Storage temperature [°C]	20
Drying	Gas velocity [m/s]	3
	Tile heat transfer coefficient [W/m^2K]	0.5
Pressing	Density of the atomized powder (ρ) [g/cm^3]	2.65

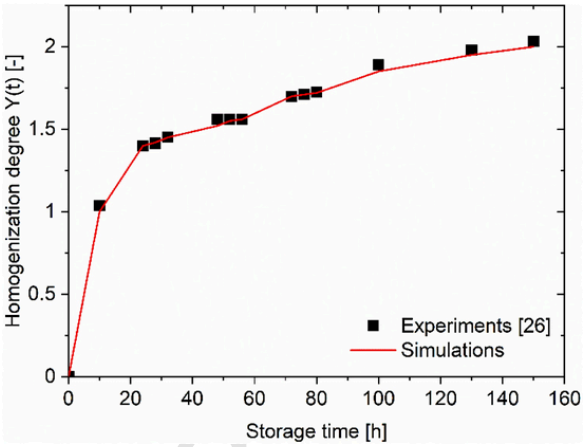

Fig. B1. Dependency of homogenization degree on storage time. Experimental data from Demarch et al [26].

$$Y(t) = \Delta U(0) - \Delta U(t) \quad \text{(B 1)}$$

where $\Delta U(0)$ and $\Delta U(t)$ are the moisture differences between coarse and fine particles in the initial storing time 0 and storing time t, respectively. When $\Delta U(t)$ reaches the minimum value or close to zero, the homogenization degree is highest. Fig. B2 illustrates the evolution of moisture fraction during storage for different granules size. Over time, the moisture difference between granules diminishes. The highest difference can be observed in the first 24 h of storage. After 48 h of storage time, $\Delta U(t)$ is approximately 0.58%, which is considered acceptable for industrial applications [26]. After 100 h, the difference can be considered as negligible.

Appendix C. Pressing parameters

Experimental data from two Brazilian factories "Eliane Revestimentos Cerâmicos" (Factory A) and "Cecrisa Revestimentos Cerâmicos" (Factory B) [31] has been used to validate the model given in Eq. (16). The different moisture of granules and applied pressures are listed in Table C1.

The model parameters A_2 and B_2 given in Eq. (16) have been proven to depend on the moisture of the granules and pressures applied during pressing. To describe this dependency the second order surface has been fitted to experimental data, which allow us to reach a good

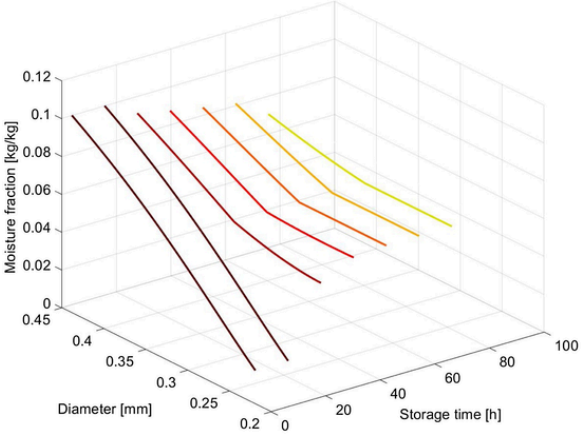

Fig. B2. Time-dependent evolution of moisture distribution among granules with different size during storage.

UNCORRECTED PROOF

Table C1
Experimental data sets for different moisture of granules and pressures applied [31].

Parameter set	Moisture of granules – Factory A [%]	Moisture of granules – Factory B [%]	Pressure – Factory A [MPa]	Pressure – Factory B [MPa]
1	7.7	6.7	19.02	36.28
2	6.5	6.0	15.49	24.91
3	6.9	6.4	17.26	30.69
4	8.1	7.1	20.69	42.07
5		7.5		47.66

agreement with a R^2 value of 0.99. The values of A_2 and B_2 and surface fitting can be seen in Figs. C1 and C2, respectively.

Appendix D. Drying model and its parameters

The diffusivity constant in Eq. (18) has been estimated based on experimental data of the factories listed in Table D1. The values attained for the diffusivity constant are shown in Fig. D1. It is assumed that the diffusivity constant can be predicted by the Arrhenius equation as:

$$D = D_0 exp\left(\frac{-Q_d}{RT}\right) \quad (D.1)$$

By linear interpolation of data from factories 1 and 3, it is possible to acquire the values for the pre-exponential factor D_0 and activation energy Q_d. Table D2 displays the obtained values. The average values of 0.116 m^2/s and 64.25 kJ/mol were adopted in the model.

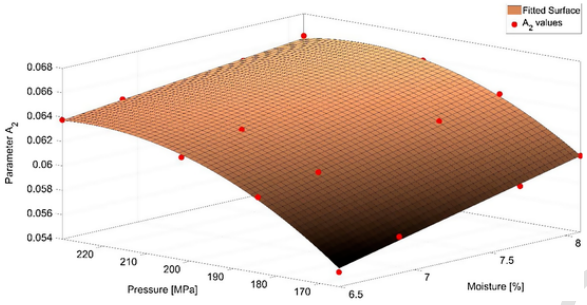

Fig. C1. Dependency of parameter A_2 on the moisture of granules and pressure applied during pressing.

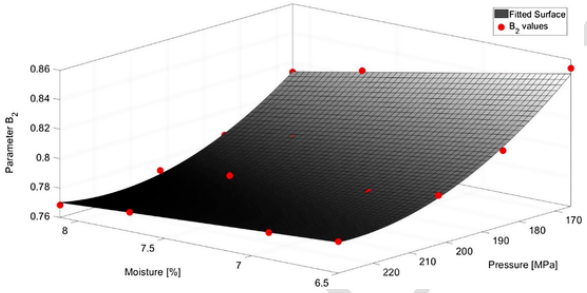

Fig. C2. Dependency of parameter B_2 on the moisture of granules and pressure applied during pressing.

Table D1
Experimental data from several Brazilian factories.

Factory	Gas temperature [K]	Residence time [s]	Tile thickness [mm]	Moisture input [%]	Moisture output [%]
1	473.15	2700	10	6.5	0.5
	458.15	3900	9	6.5	0.5
2	523.15	1500	12	7	0.3
3	408.15	1320	11	7.2	0.39
	398.15	1620	9.8	7	0.38

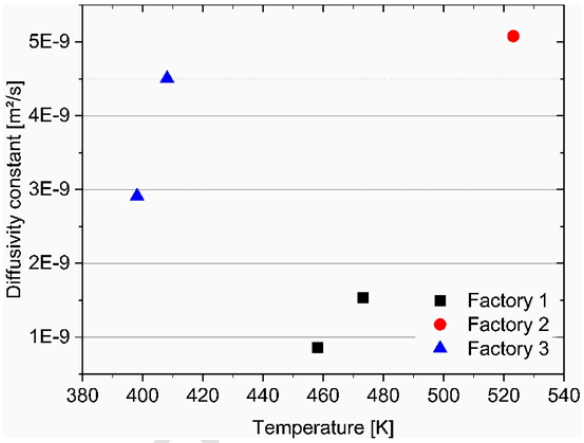

Fig. D1. Dependency of estimated diffusivity constant on temperature.

By linear interpolation of data from factories 1 and 3, it is possible to acquire the values for the pre-exponential factor D_0 and activation energy Q_d. Table D2 displays the obtained values. The average values of 0.116 m^2/s and 64.25 kJ/mol were adopted in the model.

Appendix E. Sintering parameters

Aiming to obtain the model parameters (n, k and E_a) used in Eqs. (20) and (21), experiments with optical dilatometry have been performed. The dataset of expansion has been obtained applying different constant heating rates (10 °C/min, 30 °C/min and 50 °C/min) on samples with two different median particle sizes (7.5 and 5 μm). By assuming that during sintering the linear shrinkage occurs homogeneously, it is possible to correlate shrinkage with the porosity of the samples. Fig. E1 shows the porosity variation with temperature of the samples for the different constant heating rates applied. The values of the parameters obtained for every case simulated and the quality of the fit estimated (according to the R^2 value) can be seen in Table E1.

A good agreement between the experimental dataset and model has been achieved for different conditions with a minimum R^2 value of 0.98. The main variations occur on the value of the time factor parameter n ranging from 1.033 to 2.652. The average value of 1.8425 has been adopted for the model.

Appendix F. Process parameters for Composition 2

The process parameters for *Composition 2* have been chosen according to the investigation carried out by Taskiran et al. [47,48]. In their work, the composition has been prepared on batches of 1 kg milled in a mill of 5 l porcelain pot containing 70 alumina balls of approximately 15 mm. The milling times have been varied for 3, 12, 24, 48 and 96 h. The produced slurry has been dried at 110 °C. These dried powder cakes have been broken up forming powder that have been granulated by spray drying. Given the lack of information regarding the spray dry-

Table D2
Values of pre-exponential factor (D_0) and activation energy (Q_d) for factories 1 and 3.

Factory	D_0 [m^2/s]	Q_d[J/mol]
1	0.072172	69504.69
3	0.159797	58995.61

UNCORRECTED PR

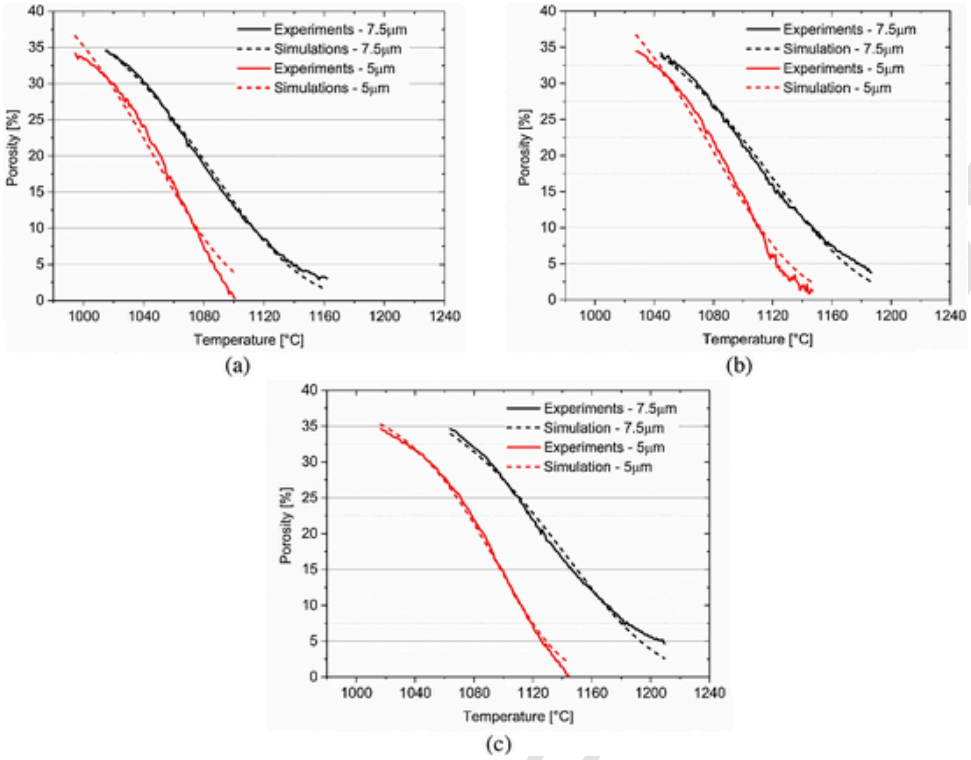

Fig. E1. Comparison between experimental data and simulation results for samples with median particles size of 7.5 and 5 μm for heating rates: (a) 10 °C/min, (b) 30 °C/min and (c) 50 °C/min.

Table E1
Values obtained for the parameters k, n and E_a with respective conditions and quality of the sintering model fit.

k	n	E_a	Heating rate (°C/min)	Median particle size (μm)	R^2
6464	1.033	275,000	10	7.5	0.9963
6464	1.105	275,000	30	7.5	0.9933
6464	1.158	275,000	50	7.5	0.9904
6464	1.11	275,000	10	5	0.9794
6464	1.175	275,000	30	5	0.9869
6464	2.652	275,000	50	5	0.9967

ing process, the same conditions of the spray drying described for the simulation of *Composition 1* have been adopted.

The test samples have been produced after uniaxial compaction at 30 MPa, producing rectangular bars with unfired dimensions of 7 mm × 75 mm × 4 mm and discs with unfired diameters of 50 mm and thickness of 3.5 mm. The sintering process of the samples have been carried in Nabertherm chamber kiln at temperatures from 1150 to 1325 °C, with intervals of 25 °C, and soaking time of 3 h. The heating rate has been kept constant at 3 °C/min.

References

[1] S. Erol, A. Jäger, P. Hold, K. Ott and W. Sihn, Tangible Industry 4.0: A Scenario-based Approach to Learning for the Future of Production, *Procedia CIRP*, **54**, 2016, 13–18.
[2] L. Pitarch Monferrer, *The Ceramic Sector Digitalization*, 2017.
[3] Ade Noni, D. Hotza, V.C. Soler and E.S. Vilches, Influence of Composition on Mechanical Behaviour of Porcelain Tile. Part I: Microstructural Characterization and Developed Phases After Firing: Part I: Microstructural Characterization and Developed Phases After Firing, *Materials Science and Engineering A*, **527** (7–8), 2010, 1730–1735.
[4] S. Breitung-Faes and A. Kwade, Prediction of Energy Effective Grindding Conditions, *Minerals Engineering*, **43–44**, 2013, 36–43.
[5] S. Breitung-Faes and A. Kwade, Use of an Enhanced Stress Model for the Optimization of Wet Stirred Media Milling Processes, *Chemical Engineering & Technology*, **37** (5), 2014, 819–826.
[6] A. Demarch, A. Checinel and A.A. Noni de, Jr., Estudo da Dinâmica de Armazenamento de pó Atomizado de Massa Cerâmica em Silos Industriais. 58° Ceramic Brazilian Congress, 2014.
[7] S. Ferrer, A. Mezquita, V.M. Aguilella and E. Monfort, Beyond the Energy Balance: Exergy Analysis of an Industrial Roller Kiln Firing Porcelain Tiles, *Applied Thermal Engineering*, **150**, 2019, 1002–1015.
[8] E.E. Gültekin, G. Topateş and S. Kurama, The Effects of Sintering Temperature on Phase and Pore Evolution in Porcelain Tiles, *Ceramics International*, **43** (14), 2017, 11511–11515.
[9] W. Kriaa, S. Bejaoui, H. Mhiri, G. Le Palec and P. Bournot, Study of Dynamic Structure and Heat and Mass Transfer of a Vertical Ceramic Tiles Dryer Using CFD Simulations, *Heat and Mass Transfer*, **50** (2), 2014, 235–251.
[10] R. Soldati, C. Zanelli, G. Guarini, S. Fazio, M.C. Bignozzi and M. Dondi, Characteristics and Rheological Behaviour of Spray-dried Powders for Porcelain Stoneware Slabs, *Journal of the European Ceramic Society*, **38** (11), 2018, 4118–4126.
[11] H.J. Alves, F.G. Melchiades and A.O. Boschi, Effect of Spray-dried Powder Granulometry on the Porous Microstructure of Polished Porcelain Tile, *Journal of the European Ceramic Society*, **30** (6), 2010, 1259–1265.
[12] C.L. Martin, Z. Yan, D. Jauffres, D. Bouvard and R.K. Bordia, Sintered Ceramics with Controlled Microstructures: Numerical Investigations with the Discrete Element Method, *Journal of the Ceramic Society of Japan*, **124** (4), 2016, 340–345.
[13] A.P.N.D. Oliveira and D. Hotza, Tecnologia de Fabricação de Revestimentos Cerâmicos, Editora da UFSC, 2015.
[14] R. Soldati, C. Zanelli, G. Guarini, A. Piancastelli, C. Melandri, S. Fazio, M.C. Bignozzi and M. Dondi, Pore Evolution and Compaction Behaviour of Spray-dried Bodies for Porcelain Stoneware Slabs, *Journal of the European Ceramic Society*, **38** (11), 2018, 4127–4136.
[15] J. Barata, F. Silva and M. Almeida, Ceramic Industry 4.0: Paths of Revolution in Traditional Products, *In Technological Developments in Industry 4.0 for Business Applications*, 2019, 278–303.
[16] M. Dosta, J.D. Litster and S. Heinrich, Flowsheet Simulation of Solids Processes: Current Status and Future Trends, *Advanced Powder Technology*, **31** (3), 2020, 947–953.
[17] V. Skorych, M. Dosta, E.-U. Hartge and S. Heinrich, Novel System for Dynamic Flowsheet Simulation of Solids Processes, *Powder Technology*, **314** (665–679), 2017, 665–679.
[18] V. Skorych, N. Das, M. Dosta, J. Kumar and S. Heinrich, Application of Transformation Matrices to the Solution of Population Balance Equations, *Processes*, **7** (8), 2019, 535.

UNCORRECTED PROOF

[19] V. Skorych, M. Dosta and S. Heinrich, Dyssol—an Open-source Flowsheet Simulation Framework for Particulate Materials, *SoftwareX*, **12**, 2020, 100572.
[20] M. Stosch von, R. Oliveira, J. Peres and S. Feyo de Azevedo, Hybrid Semi-Parametric Modeling in Process Systems Engineering: Past, Present and Future, *Computers & Chemical Engineering*, **60**, 2014, 86–101.
[21] G.R. Thorpe, Moisture Diffusion Through Bulk Grain Subjected to a Temperature Gradient, *Journal of Stored Products Research*, **18** (1), 1982, 9–12.
[22] Morrell, Power Draw of Wet Tumbling Mills and its Relationship to Charge Dynamics: Part 1: a Continuum Apprach to a Mathematical Modelling of Mill Power Draw, *Mineral Processing and Extractive Metallurgy*, **105**, 1996, C43–C53.
[23] M. Ali, T. Mahmud, P.J. Heggs, M. Ghadiri, D. Djurdjevic, H. Ahmadian, L.Mde Juan, C. Amador and A. Bayly, A One-dimensional Plug-flow Model of a Counter-Current Spray Drying Tower, *Chemical Engineering Research and Design*, **92** (5), 2014, 826–841.
[24] J. Broadhead, S.K. Edmond Rouan and C.T. Rhodes, The Spray Drying of Pharmaceuticals, *Drug Development and Industrial Pharmacy*, **18** (11–12), 1992, 1169–1206.
[25] K. Masters, Spray Drying: An Introduction to Principles Operational Practice and Applications, London, 1972.
[26] A. Demarch, Estudo da Dinâmica de Armazenamento de pó Atomizado de Massa Cerâmica em Silos Industriais. Undergraduate thesis, Criciúma, 2012.
[27] I. Zbiciński and X. Li, Conditions for Accurate CFD Modeling of Spray-drying Process, *Drying Technology*, **24** (9), 2006, 1109–1114.
[28] M.Y. Balshin, Theory of Compacting, *Metalloprom*, **18** (16), 1938, 124–137.
[29] T. Çomoglu, An Overview of Compaction Equations, 2007, Ankara Üniversitesi Eczacılık Fakültesi Dergisi, 123–134, 36.
[30] C.G. Conceição, Estudo Comparativo entre Aquecimento Ultrarápido e Convencional na Queima de Porcelanato. Master thesis, Florianópolis, 2014.
[31] Noni Junior and A. de, Modelagem Matemática Aplicada ao Controle Dimensional de Placas Cerâmicas de Monoqueima Processadas por via Úmida. Master thesis, Florianópolis, 2005.
[32] Z. Erbay and F. Icier, A Review of Thin Layer Drying of Foods: Theory, Modeling, and Experimental Results, *Critical Reviews in Food Science and Nutrition*, **50** (5), 2010, 441–464.
[33] A.S. Mujumdar, Handbook of Industrial Drying, Revised and Expanded, vol. 2 ed., 1995, CRC Press.
[34] R.H. Perry, D.W. Green and J. Maloney, *Perry's Chemical Engineers' Handbook*, 1934, McGraw-Hill handbooks.
[35] R. Riedel and I.W. Chen, Ceramics Science and Technology: Volume 3: Synthesis and Processing, 2011, John Wiley & Sons.
[36] Roger Brian Keey, Drying: Principles and Practice, 1975, Pergamon Press; Oxford.
[37] A. Sander, D. Skansi and N. Bolf, Heat and Mass Transfer Models in Convection Drying of Clay Slabs, *Ceramics International*, **29** (6), 2003, 641–653.
[38] G.R. Thorpe, Moisture Diffusion Through Bulk Grain Subjected to a Temperature Gradient, *Journal of Stored Products Research*, **18** (1), 1982, 9–12.
[39] R.Pde Gusmão, T.A. Souza Gusmão, M.E. Rangel, M. Cavalcanti-Mata and M.E. Martins Duarte, Mathematical Modeling and Determination of Effective Diffusivity of Mesquite During Convective Drying, *AJPS*, 07 (6), 2016, 814–823.
[40] S.M. Hendorson, Grain Drying Theory (I) Temperature Effect on Drying Coefficient, *Journal of Agricultural Engineering Research*, **6** (3), 1961, 169–174.
[41] K. Khalili, M. Bagherian and S. Khisheh, Numerical Simulation of Drying Ceramic using Finite Element and Machine Vision, *Procedia Technology*, **12**, 2014, 388–393.
[42] J.H. Perry, Chemical Engineers' Handbook, third ed., 1950, McGraw-Hill Book Co.; New York.
[43] S.Y. Gómez and D. Hotza, Predicting Powder Densification During Sintering, *Journal of the European Ceramic Society*, **38** (4), 2018, 1736–1741.
[44] Vasyl Skorych, Maksym Dosta and Stefan Heinrich, Dyssol—an Open-source Flowsheet Simulation Framework for Particulate Materials, *SoftwareX*, **12**, 2020, 100572.
[45] D.S. Barbosa, Controle do Tamanho Final de Porcelanatos: Modelagem e Simulação das Etapas de de Prensagem e Secagem. PhD thesis, Florianópolis, 2011.
[46] R.D. Darolt, M. Cargnin, M. Peterson and Ade Noni, Additional High-energy Milling to Enhance the Performance of Porcelain Stoneware Manufacturing, *International Journal of Applied Ceramic Technology*, **17** (4), 2020, 1742–1751.
[47] M.U. Taskiran, N. Demirkol and A. Capoglu, A New Porcelainised Stoneware Material based on Anorthite, *Journal of the European Ceramic Society*, **25** (4), 2005, 293–300.
[48] M.U. Taskiran, N. Demirkol and A. Capoglu, Influence of Mixing/milling on Sintering and Technological Properties of Anorthite based Porcelainised Stoneware, *Ceramics International*, **32** (3), 2006, 325–330.
[49] A.W. Dowling and L.T. Biegler, A Framework for Efficient Large Scale Equation-Oriented Flowsheet Optimization, *Computers & Chemical Engineering*, **72**, 2015, 3–20.
[50] C. Tsay, R.C. Pattison, M.R. Piana and M. Baldea, A Survey of Optimal Process Design Capabilities and Practices in the Chemical and Petrochemical Industries, *Computers & Chemical Engineering*, **112**, 2018, 180–189.
[51] K. Ishizaki, S. Komarneni and M. Nanko, Powder Compacts and Green Bodies for Porous Materials, *Microporous and Mesoporous Materials*, **4**, 1998, 12–37.
[52] R.E. Carter, Chapter 3 Kinetic Models for Solid State Reactions, *The Journal of Chemical Physics*, **86** (6), 1961, 75–115.
[53] J.L. Amorós, M.J. Orts, J. García-Ten, A. Gozalbo and E. Sánchez, Effect of the Green Porous Texture on Porcelain Tile Properties, *Journal of the European Ceramic Society*, **27** (5), 2007, 2295–2301.
[54] V. Beltrán, C. Ferrer, V. Bagán, E. Sánchez, J. Garcia and S. Mestre, Influence of pressing powder characteristics and firing temperature on the porous microstructure and stain resistance of porcelain tile. Qualicer 96. IV World Congress on Ceramic Tile Quality, *General Conferences and Communications Pt. 1. Castellon*, **10** (13), 1996.
[55] Ade Noni, D. Hotza, V.C. Soler and E.S. Vilches, Influence of Composition on Mechanical Behaviour of Porcelain Tile. Part II: Mechanical Properties and Microscopic residual stress, *Materials Science and Engineering A*, **527** (7–8), 2010, 1736–1743.
[56] H. Tanaka, S. Fukai, N. Uchida, K. Uematsu, A. Sakamoto and Y. Nagao, Effect of Moisture on the Structure and Fracture Strength of Ceramic Green Bodies, *Journal of the American Ceramic Society American Ceramic Society*, **77** (12), 1994, 3077–3080.
[57] M. Cargnin, S.M.A.G. Ulson de Souza, A.A. Ulson de Souza and A. Noni de, Jr., Modeling and Simulation of the Effect of the Firing Curve on the Linear Shrinkage of Ceramic Materials: Laboratory Scale and Industrial Scale, *Brazilian Journal of Chemical Engineering*, **32** (2), 2015, 433–443.
[58] G.L. Messing and A.J. Stevenson, Materials Science. Toward Pore-free Ceramics, *Science*, **322** (5900), 2008, 383–384.
[59] C. Zanelli, M. Raimondo, M. Dondi, G. Guarini and P. Tenorio, Sintering Mechanisms of Porcelain Stoneware Tiles, *M. o. Qualicer*, 2004, 247–259.
[60] M. Dosta, K.P. Furlan, V. Skorych, S. Heinrich and R. Janssen, Influence of Pores Arrangement on Stability of Photonic Structures During Sintering, *Journal of the European Ceramic Society*, **40** (13), 2020, 4562–4571.

UNCORRECTED PROOF